1-27-2012

Size effects in NiTi from density functional theory calculations

Karthik Guda Vishnu
Purdue University, karthikguda@purdue.edu

Alejandro Strachan
Birck Nanotechnology Center, Purdue University, strachan@purdue.edu

Follow this and additional works at: http://docs.lib.purdue.edu/nanopub

Part of the Nanoscience and Nanotechnology Commons

Size effects in NiTi from density functional theory calculations

Karthik Guda Vishnu[1,*] and Alejandro Strachan[1,2]

[1]*School of Materials Engineering, Purdue University, West Lafayette, Indiana 47907, USA*
[2]*Birck Nanotechnology Center, Purdue University, West Lafayette, Indiana 47907, USA*

We use density functional theory to characterize how size affects the relative stability of thin NiTi slabs of different crystal structures and its implication on the martensitic phase transition that governs shape memory. We calculate the surface energies of B2′ phase (austenite), B19 (orthorhombic), B19′ (martensite), and a body-centered orthorhombic phase, the theoretically predicted ground state. We find that $(110)_{B2}$ surfaces with in-plane atomic displacements stabilize the austenite phase with respect to B19′ and BCO; thus, slabs with such orientations are predicted to exhibit a decrease in martensite transition temperature with decreasing thickness. Our calculations predict a critical thickness of 2 nm, below which the transition would not occur. The opposite trend is observed in slabs with atomic displacements along the surface normal: the phase transformation temperature increases with decreasing size.

I. INTRODUCTION

Shape memory materials are an important class of active materials with wide range of applications. They are used in medicine as implant devices due to their excellent biocompatibility, as damping devices and mechanical actuators.[1] Their name originates from the fact that after inelastic deformation these materials recover their original shape upon heating. The shape memory behavior is due to a solid-solid, diffusionless phase transformation (called martensitic) between a high-temperature phase (austenite) and a low-temperature phase (martensite). Usually, the martensitic phase has lower symmetry than austenite, and shape memory is possible when the symmetry groups of both austenite and martensite are included in a common finite symmetry group[2] and when the transformation is atomistically reversible, i.e., all the variants of martensite transform to a unique austenite variant upon heating.[3] Scaling specimen size down to the nanoscale leads to significant changes in the thermomechanical response of these materials, and recent theoretical predictions[3] indicate that NiTi, the most widely used shape memory alloy (SMA), may lose its memory effect entirely at the nanoscale. Thus a fundamental understanding of the atomic level mechanisms that govern the response of SMA and its size effects, including the role of free surfaces, interfaces, and nanostructure[4] is critical both from the applied and basic science points of view.

The martensitic transformation can be either thermally or mechanically induced and is characterized by a critical temperature and a critical stress. For macroscopic polycrystalline samples with grain sizes larger than approximately 100 μm,[5–8] the critical transformation temperature is a function of composition alone and relatively independent of microstructure and cooling rate. However, for nanoscale and nanostructured materials, surfaces and interfaces play a large role and affect the phase transition temperature. Experimental studies on nanocrystalline NiTi revealed strong size effects for grain sizes in the range of 50 to 350 nm.[9] For samples with a mean grain diameter of approximately 60 nm and with 90% of the grains smaller than 100 nm, the martensite start (M_s) and martensite finish (M_f) transformation temperatures decrease from 330 to 319 K and from 302 K to less than 197 K, respectively, when compared to a coarse grained polycrystalline sample. Transmission electron microscopy (TEM) studies show that grains with diameters less than 50 nm fail to transform to martensite even after quenching to 197 K. Experimental studies by Glezer and collaborators[10] on $Ni_{50}Ti_{25}Cu_{25}$ nanoparticles embedded in an amorphous matrix show similar trends for the B2–B19 martensite phase transformation. The authors find either partially or fully suppressed transformation at sizes less than 25 nm and indicate that for spheres of diameter less than 16 nm, the martensite transformation is completely suppressed. In the case of Fe-Ni-B alloys, the authors show that the martensite transformation is not completely suppressed, but the critical transformation temperature is reduced to as low as 4.2 K. Similar trends have been observed in fine cobalt powders,[11] polycrystalline samples of low-alloy steels,[12] Au-Cd,[13] and Fe-Ni systems.[14] Size also affects the mechanical response of shape memory materials. Submicrometer pillars of Cu-Ni-Al SMAs show extraordinarily large mechanical hysteresis,[15] a fact that could be exploited for applications requiring high mechanical damping. Several mechanisms have been postulated to contribute to such size effects, including surface and interfacial energies, mechanical constraints, and the resulting changes in the martensite microstructure.[4,16,17] Surfaces are also known to drive phase transformations in nanoscale face-centered-cubic (fcc) wires.[18–20] Molecular dynamics (MD) simulations showed that surface stresses cause $\langle 100 \rangle$ nanowires to spontaneously change their orientation to $\langle 110 \rangle$ in Ni, Ag, and Cu; in the case of Au nanowires with diameters less than 2 nm, a transformation to a body-centered tetragonal structure has been observed.[18] Furthermore, Cu and Ni square cross-section nanowires also exhibit shape memory and pseudoelasticity because of the above-mentioned structural relaxations and their large stacking fault energies.[21] Gold nanofilms of thickness less than 2 nm (eight atomic layers) have also been experimentally observed to transform from the (001) orientation to (111) spontaneously.[22] These findings emphasize that surface properties are extremely important to understand the stability of phase transformations

in nanoscale specimens. An understanding of the role of free surfaces and interfaces on the structural transformations and properties of NiTi and related SMAs is lacking. This knowledge is critical to understand the size effects in shape memory and pseudoelasticity for these materials, and this paper focuses on the role of free surfaces on the relative energetics of thin NiTi slabs of various crystal structures.

In this paper we use density functional theory (DFT) to predict the surface energy of the various phases that play a role in NiTi shape memory: B2′, B19, B19′, and BCO. In equiatomic NiTi the high-temperature, austenite phase is B2; however, B2 is known to be unstable with respect to atomic displacements along the [110] direction at zero temperature; the resulting phase, denoted B2′,[23,24] will be taken in this paper as the high-temperature austenite phase. B19 is an orthorhombic phase observed in this system when Cu is present as an impurity. The monoclinic B19′ is the experimentally observed martensite structure. However, recent DFT calculations,[3] predict a different phase, body-centered orthorhombic (BCO), to be the ground state of this system. This finding is important because the B2-BCO-B2 phase transformation is not atomistically reversible and hence would not result in shape memory. These results were later confirmed in various *ab initio* studies, and transformation paths between the above phases[24–26] and free-energy barriers[27] were studied. However, the BCO phase has still not been confirmed experimentally, and the B19′ phase may be stabilized by internal stresses that developed during the martensitic transformation.[24] Our results show that free-surface energies affect the relative stability of the various phases in thin NiTi slabs in a significant way and under certain circumstances can arrest the martensite phase transition.

The remainder of the paper is organized as follows: Sec. II describes simulation details; Sec. III describes how surface energies vary across different phases and different slab thicknesses. In Sec. IV we discuss the structures of relaxed slabs, and in Sec. V we discuss how size influences the relative energetics of NiTi slabs. Finally, in Sec. VI we present a summary and our conclusions.

II. SIMULATION DETAILS

A. DFT calculations

Simulations have been carried out using SeqQuest,[28–30] a DFT[31] code developed at Sandia National Laboratories, within the generalized gradient approximation (GGA) of Perdew, Burke, and Ernzerhof (PBE).[32] SeqQuest uses contracted Gaussian functions as a basis set, and our calculations are performed using double-zeta polarization basis sets. Norm-conserving pseudopotentials of the Hamann-type,[33] parameterized for the PBE functional, are used. All our calculations are spin independent and are performed at a 0.04-eV electronic temperature. SeqQuest uses the maximum change in any Hamiltonian matrix element as its convergence criterion; this has been set to be 2.72×10^{-4} eV for all calculations. All the slab structures have been fully relaxed with respect to atoms using the Broyden method.[34] Convergence was assumed when the absolute value of the atomic force on every atom was less than or equal to 25×10^{-3} eV/Å. Fourteen and 10

k-points are used in the **a** and **b** periodic directions (described below) and 3, 2, and 1 k-points are used in the nonperiodic direction for the 3-, 5-, and 7-unit-cell slab structures described below.

To verify the robustness of our predictions, we repeated our surface energy calculations for the largest slabs (7 unit cells) with Quantum Espresso (QE),[35] a plane-wave DFT[31] code. We use ultrasoft pseudopotentials[36] parameterized for PBE[32] within the generalized gradient approximation for both Ni and Ti. For our calculations we used a cutoff of 762 eV for the plane-wave expansion of the wave functions and 7,620 eV for charge density. The first Brillouin zone is sampled using a Monkhorst-Pack grid centered at the Γ point. Fourteen and 10 k-points are used in the periodic direction, whereas 1 k-point is used to sample the nonperiodic direction. We used the Methfessel-Paxton[37] technique for smearing with a smearing parameter of 0.04 eV. Convergence criterion for the self-consistent field calculation is set at 1×10^{-8} Ry, and the mixing factor is set at 0.3. All our slab structures have been fully relaxed with respect to atom positions using the Broyden-Fletcher-Goldfarb-Shanno[38–41] minimization method, and the convergence was assumed when all the components of the force vector on every atom are less than or equal to 25×10^{-3} eV/Å. All our calculations are spin independent.

B. Initial slab structures

The initial slab structures are prepared starting from the fully relaxed DFT-GGA crystal structures of different phases from our earlier work.[24] All our unit cells are oriented with lattice parameter **a** parallel to $[100]_{B2}$, **b** along $[110]_{B2}$, and **c** along $[-110]_{B2}$ of the B2 crystal structure. The unit cells are replicated three, five, and seven times in the direction normal to the surface of interest, and two free surfaces are created using a vacuum of 12.70 Å; periodic boundary conditions are imposed in all three directions. These types of boundary conditions are commonly used in surface energy calculations; see, for instance, Ref. 42. This corresponds to an infinite number of slabs periodic in two dimensions (2D) and separated by a vacuum region sufficiently thick for the interactions between slab replicas to be negligible. To verify this, we performed simulations with 2D periodic boundary conditions and open boundaries along c and found free-surface energy differences of about 1%. All our calculations focus on low-energy $(110)_{B2}$ surfaces. Because the B2′, B19, B19′, and BCO crystal structures exhibit atomic displacements with respect to the high-symmetry B2 configuration, two $(110)_{B2}$ surfaces are possible in each case; one in which atomic displacements are normal to the free surface (denoted hereafter out of plane) and one in which bulk displacements are parallel to the free surface (in-plane surfaces). In the case of out-of-plane surfaces, we studied both Ti-terminated (Ti-out) and Ni-terminated (Ni-out) surfaces, see Fig. 1. To obtain relaxed surface structures and energies, we start from the bulk structure and minimize the total energy with respect to atomic positions, keeping the transverse lattice parameters fixed. No symmetry is imposed in any of the calculations.

For the QE calculations we use the lattice parameters of Huang *et al.*,[3] for all phases corresponding to the GGA-Ultra soft pseudopotentials (USPP) flavor of DFT; after atomic
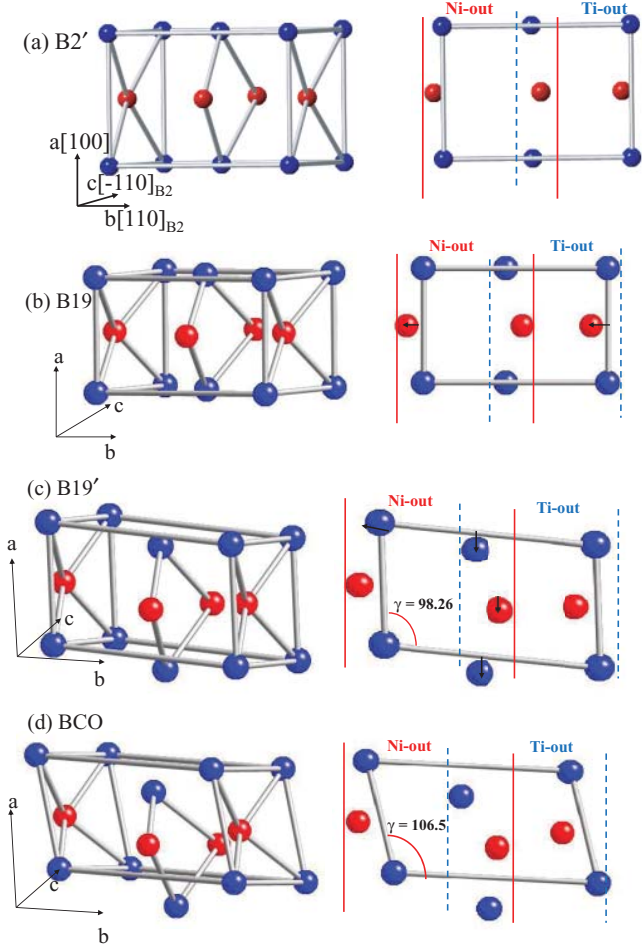
FIG. 1. (Color online) Snapshots of various crystal structures of NiTi and an in-plane view of how the Ni-terminated and the Ti-terminated [110] surfaces are cleaved. (a) B2′, (b) B19, (c) B19′ (martensite), and (d) BCO. Ti and Ni atoms are indicated by blue and red spheres, respectively.

relaxation, the stress components in the structures are no larger than −0.87 GPa, indicating the appropriateness of the lattice parameters chosen. The initial slab structures are built the same way as the SeqQuest structures, and the surface energies and relaxed structures are found by relaxing these structures with respect to atomic positions, keeping the lattice parameters fixed.

III. SURFACE ENERGY OF THIN NITI SLABS

Surface energy (γ) is calculated from the total energy of the relaxed slab and that of the perfect crystal structure as

$$\gamma^\alpha = \frac{E_{\text{Slab}}^\alpha(N) - N \cdot n_{uc}^\alpha \cdot E_{\text{Bulk}}^\alpha}{2 \times A^\alpha},\qquad(1)$$

where the superscript α denotes the crystal structure, $E_{\text{Slab}}^\alpha(N)$ is the total energy of a slab consisting of N unit cells, E_{Slab}^α is the energy of the corresponding bulk per formula unit, n_{uc}^α is the number of formula units per unit cells, and A^α is the corresponding cross-sectional area. For completeness, Table I summarizes the bulk lattice parameters and cohesive energies per formula unit for each phase predicted from our DFT-GGA calculations,[24] using SeqQuest, previous *ab initio* calculations,[3] using plane waves and ultrasoft pseudopotentials (whose lattice parameters we use for the QE calculations) and experimental values that show the accuracy of the *ab initio* predictions.

Figure 2 shows surface energies for all crystals and surface types as a function slab thickness. Very weak size dependence is observed; the change in surface energy going from slabs thickness of 3 to 7 unit cells is less than 2% for any of the cases studied. Out-of-plane energies in all cases correspond to the Ti-terminated structures as these are found to be the low-energy configurations. For both surface types, the B2′ crystal has the lowest surface energy among all phases, followed by B19, B19′, and BCO. Our calculations using QE (with a different basis set and pseudopotentials as compared with SeqQuest) lead to similar energetics; the difference in surface energies for the two approaches is between 5 and 11% of each other.
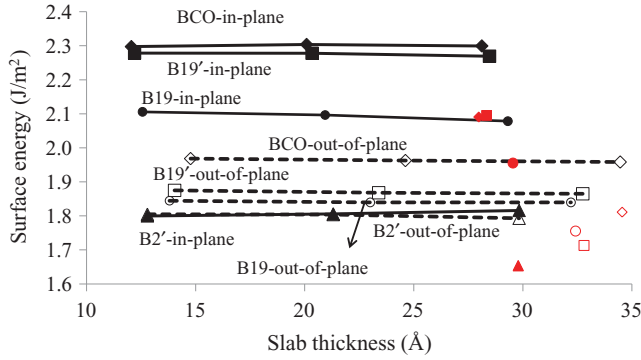
TABLE I. Lattice parameters (Å) and cohesive energies (per formula unit) of B2, B2′, B19, B19′, and BCO from our calculations as well as from previous theoretical and experimental works. DFT-GGA refers to SeqQuest calculations and GGA-USPP refers to QE calculations using lattice parameters from Ref. 3.

Phase	Method	a (Å)	b (Å)	c (Å)	Monoclinic cell angle (°)	E–E$_{B2}$ (eV)
	DFT-GGA	3.011	4.258	4.258	90.0	0.000
B2	GGA-USPP	3.009	4.255	4.255	90.0	0.000
	Exp[43]	3.014	4.262	4.262	90.0	0.000
B2′	DFT-GGA	3.011	4.258	4.258	90.0	−0.009
	GGA-USPP	3.009	4.255	4.255	90.0	−0.005
B19	DFT-GGA	2.850	4.597	4.167	90.0	−0.051
	GGA-USPP	2.776	4.631	4.221	90.0	−0.046
B19′	DFT-GGA	2.933	4.678	4.065	98.26	−0.081
	GGA-USPP	2.929	4.686	4.048	97.78	−0.075
	Exp[44]	2.898	4.646	4.108	97.8	–
	DFT-GGA	2.926	4.925	4.012	106.5	−0.097
BCO	GGA-USPP	2.940	4.936	4.012	107.0	−0.081
	GGA-USPP[3]	2.940	4.936	3.997	107.0	−0.1

FIG. 2. (Color online) Surface energy as a function slab thickness for the various crystal structures and orientations. Symbols joined by lines represent SeqQuest results (dashed lines are used for out-of-plane displacements and solid lines for in-plane cases. Light symbols (red online) correspond to surface energy calculations using QE for the largest slab size considered to assess the accuracy of the predictions.

For both kinds of surfaces, the relative order of some of the surface energies change, but the values are similar. As will be discussed in detail below, this difference in surface energy causes the relative stability of the NiTi slabs with different phases to be size dependent.

We are unaware of the experimental characterization of the surface energy of NiTi to validate our predictions, but the measurements for liquid NiAl[45,46] give 1.4 J/m^2 at a temperature just above the melting temperature. DFT calculations in B2 NiTi by Nolan *et al.*[47] predict a surface energy of 1.05 J/m^2 for the (110) surface for a slab of thickness 19.5 Å. Our calculations predict larger surface energies: 1.80 J/m^2, for SeqQuest a slab of similar thickness (21 Å), and 1.65 J/m^2 for QE. The origin of this discrepancy is unclear at this

point; even if we use B2 as the reference structure, we obtain larger surface energies than those in Ref. 47. The systematic agreement between SeqQuest and QE simulations across sizes and structures support the accuracy of our results.

Interestingly, the relative surface energies of the various phases can be explained by a simple analysis of broken bonds. Table II lists (i) the first nearest neighbors and their distance for all the phases in bulk form, (ii) the bonds that are broken while creating each of the surfaces, and (iii) their surface energies corresponding to the SeqQuest and QE results for the 7-unit-cell-thick slabs. As described earlier, at zero temperature the B2 phase is unstable with respect to atomic displacements in the [110] direction, thus the eight first nearest neighbors in B2 separate into three subshells in B2′ with two pairs in the first subshell, four in the second, and the remaining two in the third. As can be seen in Table II, for each crystal structure the lowest energy surface is the one that requires breaking the longest bonds. Table II also shows that the increase in surface energy from B2′ to B19, followed by B19′ and BCO, also correlates with the number of broken bonds. For example, creating an in-plane surface in B2′ involves breaking two NiTi bonds of intermediate length, but in B19, B19′, and BCO the lattice distortions and atomic displacements bring additional bonds within the range of the first nearest neighbors and breaking those leads to higher surface energies. In the case of out-of-plane surfaces, the bond-counting analysis is inconclusive. Although this bond-counting analysis ignores surface relaxation, it provides insight into the trends observed even after full relaxation for in-plane surfaces.

IV. STRUCTURES OF RELAXED SLABS

The structural aspects of surface relaxation can be divided into the rigid translation of atomic planes normal to the surface and atomic displacements with respect to their corresponding

TABLE II. Near neighbors, average bond distances (Å; correspond only to structures predicted by SeqQuest), and relaxed surface energies (J/m^2) for all phases (values in parentheses correspond to surface energies in eV/Å^2).

| Phase	Bulk/ surface	Neighbors and average distance (Å)					Surface energy SeqQuest J/m^2 and (eV/Å^2)	Surface energy QE J/m^2 and (eV/Å^2)
B2′	Bulk	2 Ni/Ti @ 2.53	4 Ni/Ti @ 2.62	2 Ni/Ti @ 2.69				
	In-plane		2 broken				1.81(0.113)	1.65(0.103)
	Ni-out	2 broken					1.86(0.116)	1.7(0.106)
	Ti-out			2 broken			1.79(0.112)	1.65(0.103)
B19	Bulk	2 Ni/Ti @ 2.556	4 Ni/Ti @ 2.564	2 Ni/Ti @ 2.853	2 Ti/Ni @ 2.839	2-/Ni @ 2.702		
	In-plane		2 broken			1 broken	2.08(0.130)	1.96(0.122)
	Ni-out	2 broken				2 broken	2.21(0.138)	2.05(0.128)
	Ti-out			2 broken			1.84(0.115)	1.76(0.110)
B19′	Bulk	2 Ni/Ti @ 2.568	4 Ni/Ti @ 2.559	1 Ni/Ti @ 2.62	2-/Ni @ 2.60			
	In-plane		2 broken		1 broken		2.27(0.142)	2.10(0.131)
	Ni-out	2 broken			2 broken		2.4(0.150)	2.12(0.132)
	Ti-out			1 broken			1.86(0.116)	1.71(0.107)
BCO	Bulk	2 Ni/Ti @ 2.605	4 Ni/Ti @ 2.544	1 Ni/Ti @ 2.56	2-/Ni @ 2.575			
	In-plane		2 broken		1 broken		2.3(0.144)	2.09(0.130)
	Ni-out	2 broken			2 broken		2.44(0.152)	2.23(0.139)
	Ti-out			1 broken			1.96(0.122)	1.81(0.113)
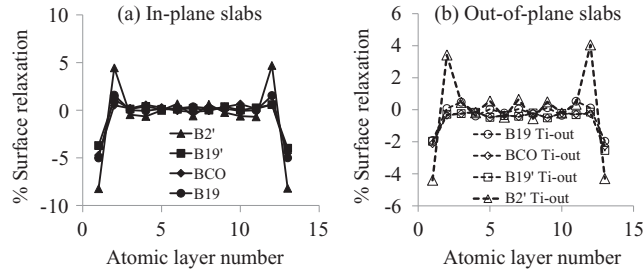
FIG. 3. Percent surface relaxation for the 7-unit-cell-thick slabs for all crystal structures. (a) In-plane slabs and (b) out-of-plane (Ti-terminated) slabs.

plane (both in the surface plane and normal to it). Figure 3 shows the percent change in interplanar separation across the slabs (results for the longest 7-unit-cell slabs are shown). Interplanar relaxation is defined as

$$\frac{\Delta_{i-i+1}^{\text{slab}} - \Delta^{\text{bulk}}}{\Delta^{\text{bulk}}}$$

$$\Delta_{i-i+1}^{\text{slab}} = COM_i - COM_{i+1}, \tag{2}$$

where i indexes each of the interplanar spacings and Δ indicates the difference in center of mass position of neighboring planes in the direction normal to the surface both for the slab and bulk. The interplanar separation distance in the bulk structures Δ^{bulk} is constant, while surface relaxation in the slabs leads to variations in this quantity as the free surface is approached. Negative values indicate contraction and positive values indicate expansion. In all cases we observe a contraction of the outermost interplanar layer followed by an expansion in the following layer. After a few layers, bulk interplanar distances are recovered, explaining the insensitivity of the surface energy to slab thickness. In both surfaces the B2′ phase exhibits significantly more relaxation that the other structures. We find between 8 and 5% contraction in the outermost layer. The relaxation is in agreement with prior DFT calculations[47] that report a relaxation of 6% for the outermost layer in B2.

We now turn our attention to the atomic relaxations with respect to their corresponding planes in the relaxed structured. Atomic displacements along the a, b, and c crystal axes are computed throughout the slab in the same way they are defined in the bulk;[24] they are measured from the symmetric atomic positions obtained from a rigid deformation of the B2 structure. For the nonperiodic direction, we evaluate atomic displacements based on an instantaneous lattice parameter for each unit cell obtained from the relaxed atomic plane positions.

Figure 4 shows the relaxed slab structures as well as atomic displacements as a function of position along the slabs' thickness for all the cases considered. As is the case for interplanar separations, B2′ exhibits larger atomic displacements than the other phases. Bulk B2′ and B19 structures exhibit displacements along the $[110]_{\text{B2}}$ direction (Y in Fig. 4), and out-of-plane surfaces affect the magnitude of these displacements near the free surface (significantly in B2′ and very little in B19) but do not lead to displacements in other directions. In contrast, in-plane B2′ and B19 surfaces lead to atomic displacements not just along $[110]_{\text{B2}}$ but also along the

surface normal $[-110]_{\text{B2}}$ (Z in Fig. 4); this new displacement is confined to the outermost unit cell in the slabs. Bulk B19′ and BCO exhibit displacements along $[110]_{\text{B2}}$ and $[001]_{\text{B2}}$, and the two surfaces modify the magnitude of these displacements but do not lead to significant displacements in the third direction; see Figs. 4(e)–4(h). Overall, B2′ and B19 surfaces lead to more pronounced structural changes that explain their lower surface energies beyond the simple bond-breaking analysis discussed above.

V. RELATIVE ENERGETICS OF THIN NITI SLABS

In this section we discuss the implications of our results on the relative stability of slabs of the various phases as a function of their thickness. Based on Eq. (1) for surface energy, we can express the energy of a slab consisting of N unit cells in terms of their bulk energy and surface energy

$$E_{\text{Slab}}^{\alpha}(N) = N \cdot n_{uc}^{\alpha} \cdot E_{\text{Bulk}}^{\alpha} + 2 \times A^{\alpha}\gamma^{\alpha}, \tag{3}$$

where the superscript α denotes the crystal structure, $E_{\text{Slab}}^{\alpha}(N)$ is the total energy of a slab consisting of N unit cells, E_{Bulk}^{α} is the energy of the corresponding bulk per unit formula, n_{uc}^{α} is the number of formula units per unit cell, A^{α} is the corresponding cross sectional area, and γ^{α} is the corresponding surface energy. Figure 5 shows the energy difference, per formula unit, between B19′ and B2′ slabs, Fig. 5(a), and BCO and B2′, Fig. 5(b), as a function of their thickness both for SeqQuest (full lines) and QE (dashed lines) surface energies. The surface energy used for the functions in Fig. 5 is that of the thickest slabs and the length reported in terms of that of the B2′ slabs. For out-of-plane (Ti-out) slabs, B19′ and BCO become more stable than B2′ as the slab thickness decreases. This result may appear surprising because B2′ has the lowest surface energy of the phases; however, as Eq. (4) shows, it is the product of a free-surface energy and cross-sectional area that governs the slab energetics. Although entropic effects should be taken into account for a definite conclusion, these results indicate that the martensite transition temperature would increase with decreasing slab thickness. For in-plane slabs, B2′ becomes more stable than B19′ and BCO with decreasing size; our results predict a critical size of 2 nm below which martensitic transformation would not occur. The accuracy of our mathematical model and the convergence of surface energies can be confirmed from Fig. 5, where the actual DFT calculations (points) are compared with the model (lines). Our model indicates that the size affects the phase transformation temperature at sizes beyond the actual DFT calculations; for example, the energy difference of 20-nm-thick slabs of B19′ and B2′ phases will be 15% smaller than the energy difference in the bulk for the in-plane slabs. It is also clear that these effects will be more important in wires one-dimensional (1D) or in clusters zero-dimensional (0D).

VI. SUMMARY AND CONCLUSIONS

We used DFT-GGA to study the atomic structure and energetics of thin NiTi slabs of the various crystal structures that play a role in shape memory. We focus on the low-energy [110] surfaces of B2′, B19, B19′, and BCO crystals. We find that the high-temperature austenite phase (B2′) has the lowest
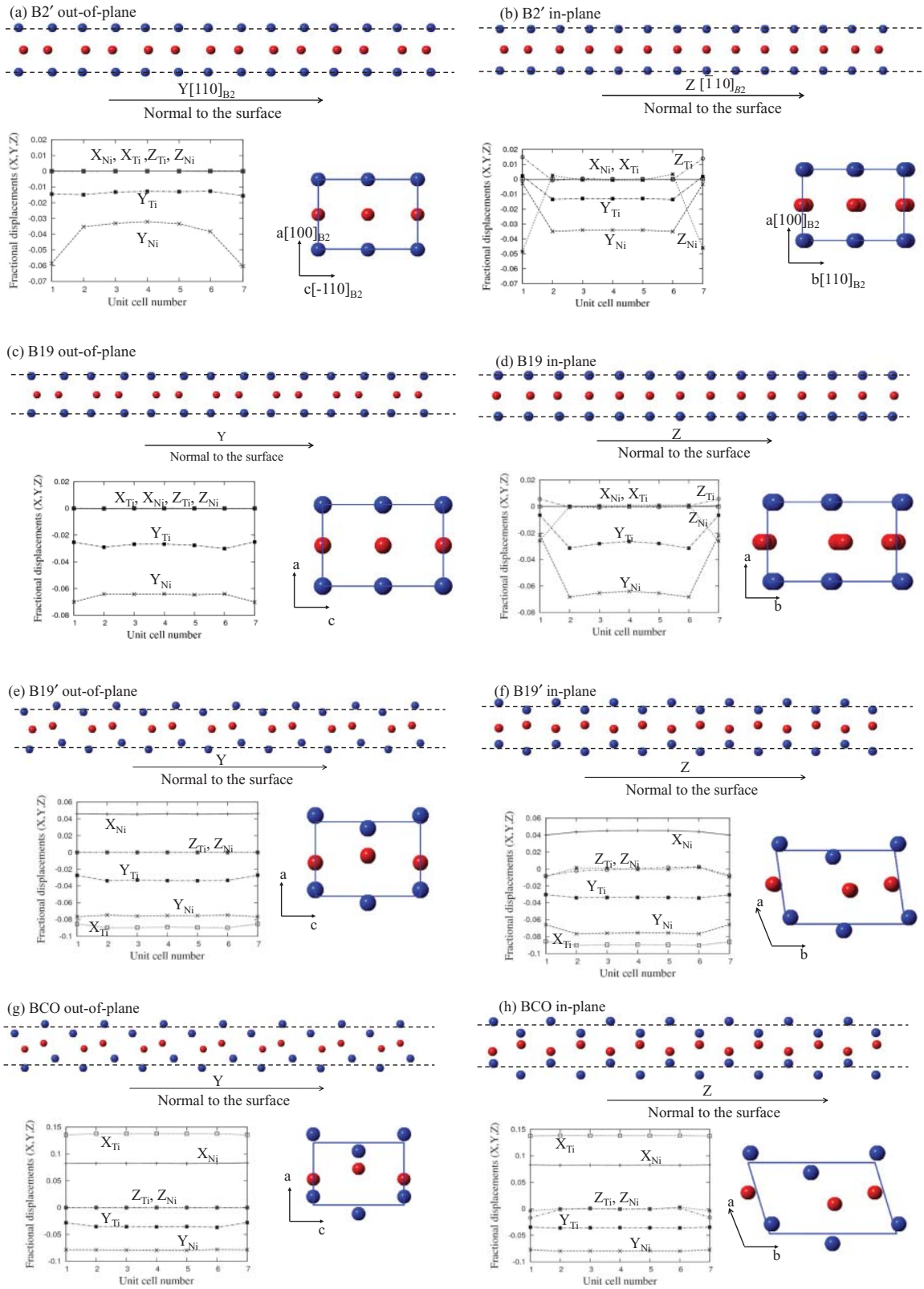
FIG. 4. (Color online) Atomic displacements of relaxed slabs (largest size) for all surfaces under consideration and snapshots of the relaxed structures (both side and cross-sectional views). (a) B2′ out-of-plane slab, (b) B2′ in-plane slab, (c) B19 out-of-plane slab, (d) B19 in-plane slab, (e) B19′ out-of-plane slab, (f) B19′ in-plane slab, (g) BCO out-of-plane slab, and (h) BCO in-plane slab.
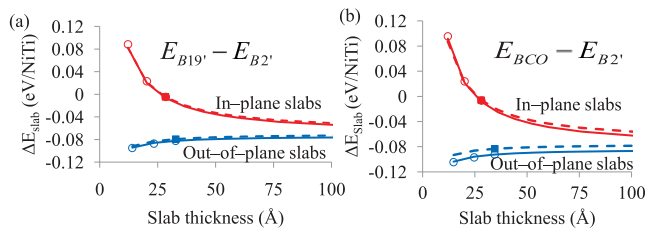
FIG. 5. (Color online) Relative phase stability of the martensite phases B19′ (a) and BCO (b) with respect to B2′. Full lines and dashed lines are model predictions using the surface energies predicted by SeqQuest and QE, respectively, points (open symbols correspond to SeqQuest calculations, and full symbol corresponds to QE calculations) represent the actual calculations.

surface energy followed by B19, B19′, and BCO. For slabs with atomic displacements parallel to the free surface, we predict a decrease in martensite transition temperature with decreasing slab thickness and a critical size of 2 nm for NiTi slabs, below which transformation would not occur. Such an inverse relationship between the critical transformation

temperature (T_c) and size (diameter) has been observed in cylindrical iron nanowires with diameters ranging from 2.5 to 4 nm.[48] In contrast, crystals with atomic displacements normal to the free surface, the martensite phases B19′ and BCO become more stable with respect to B2′ with decreasing slab thickness, indicating an increase in the transition temperature. These results indicate a complex role of free surfaces on size effects in martensite transition temperature, and additional DFT calculations on wires and spherical particles could provide important new insight. In addition, characterizing the effect of different surface passivations on the relative energy of nanoscale specimens with different crystal structure is critical to assess the potential use of NiTi and other SMAs in nanoscale applications.

ACKNOWLEDGMENTS

*Corresponding author: kgudavis@purdue.edu

[1] K. Otsuka and X. Ren, Prog. Mater. Sci. **50**, 511 (2005).

[2] K. Bhattacharya, S. Conti, G. Zanzotto, and J. Zimmer, Nature **428**, 55 (2004).

[3] X. Huang, G. J. Ackland, and K. M. Rabe, Nat. Mater. **2**, 307 (2003).

[4] A. Thompson and A. Strachan, Phys. Rev. B **81**, 085429 (2010).

[5] C. Lopez del Castillo, B. G. Mellor, M. L. Blazquez, and C. Gomez, Scr. Metall. **21**, 1711 (1987).

[6] K. Mukunthan and L. C. Brown, Metall. Trans. A **19**, 2921 (1988).

[7] P. F. Brofman and G. S. Ansell, Metall. Trans. A **14**, 1929 (1983).

[8] Y. Chen and C. A. Schuh, Acta Mater. **59**, 537 (2011).

[9] T. Waitz, T. Antretter, F. D. Fischer, and H. P. Karnthaler, Mater. Sci. Technol. **24**, 934 (2008).

[10] A. M. Glezer, E. N. Blinova, V. A. Pozdnyakov, and A. V. Shelyakov, J. Nanopart. Res. **5**, 551 (2003).

[11] O. Kitakami, H. Sato, Y. Shimada, F. Sato, and M. Tanaka, Phys. Rev. B **56**, 13849 (1997).

[12] H. Seok-Yang and H. K. D. H. Bhadeshia, Scr. Mater. **60**, 493 (2009).

[13] K. Asaki, T. Tadaki, and Y. Hirotsu, Philos. Mag. A **82**, 463 (2002).

[14] K. Asaki, Y. Hirotsu, and T. Tadaki, J. Electron Microsc. **48**, 387 (1999).

[15] J. San Juan, M. L. Nǒ, and C. A. Schuh, Nat. Nanotechnol. **4**, 415 (2009).

[16] M. Bouville and R. Ahluwalia, Acta Mater. **56**, 3558 (2008).

[17] T. Waitz, K. Tsuchiya, T. Antretter, and F. D. Fischer, MRS Bull. **34**, 814 (2009).

[18] M. I. Haftel and Ken Gall, Phys. Rev. B **74**, 035420 (2006).

[19] J. Diao, K. Gall, and M. L. Dunn, Nat. Mater. **2**, 656 (2003).

[20] J. Diao, K. Gall, and M. L. Dunn, Phys. Rev. B **70**, 075413 (2004).

[21] H. S. Park, K. Gall, and J. A. Zimmerman, Phys. Rev. Lett. **95**, 255504 (2005).

[22] Y. Kondo, Q. Ru, and K. Takayanagi, Phys. Rev. Lett. **82**, 751 (1999).

[23] X. Huang, C. Bungaro, V. Godlevsky, and K. M. Rabe, Phys. Rev. B **65**, 014108 (2001).

[24] K. Guda Vishnu and Alejandro Strachan, Acta Mater. **58**, 745 (2010).

[25] N. Hatcher, O. Yu. Kontsevoi, and A. J. Freeman, Phys. Rev. B **79**, 020202(R) (2009).

[26] N. Hatcher, O. Yu. Kontsevoi, and A. J. Freeman, Phys. Rev. B **80**, 144203 (2009).

[27] D. Mutter and P. Nielaba, Phys. Rev. B **82**, 224201 (2010).

[28] P. A. Schultz, SeqQuest Code, [http://dft.sandia.gov/Quest].

[29] P. J. Feibelman, Phys. Rev. B **35**, 2626 (1987).

[30] P. J. Feibelman, Phys. Rev. B **44**, 3916 (1991).

[31] P. Hohenberg and W. Kohn, Phys. Rev. **136**, B864 (1967).

[32] J. P. Perdew, K. Burke, and M. Ernzerhof, Phys. Rev. Lett. **77**, 3865 (1996).

[33] D. R. Hamann, Phys. Rev. B **40**, 2980 (1989).

[34] D. D. Johnson, Phys. Rev. B **38**, 12807 (1988).

[35] P. Giannozzi, S. Baroni, N. Bonini, M. Calandra, R. Car, C. Cavazzoni, D. Ceresoli, G. L. Chiarotti, M. Cococcioni, I. Dabo, A. Dal Corso, S. Fabris, G. Fratesi, S. de Gironcoli, R. Gebauer, U. Gerstmann, C. Gougoussis, A. Kokalj, M. Lazzeri, L. Martin-Samos, N. Marzari, F. Mauri, R. Mazzarello, S. Paolini, A. Pasquarello, L. Paulatto, C. Sbraccia, S. Scandolo, G. Sclauzero, A. P. Seitsonen, A. Smogunov, P. Umari, and R. M. Wentzcovitch, J. Phys. Condens. Matter **21**, 395502 (2009).

[36] D. Vanderbilt, Phys. Rev. B **41**, 7892 (1990).

[37] M. Methfessel and A. T. Paxton, Phys. Rev. B **40**, 3616 (1989).

[38] C. G. Broyden, IMA J. Appl. Math. **6**, 76 (1970).

[39] R. Fletcher, Comput. J. **13**, 317 (1970).

[40] D. Goldfard, Math. Comput. **24**, 23 (1970).

[41]D. F. Shanno, Math. Comput. **24**, 647 (1970).

[42]A. Alam, B. Kraczek, and D. D. Johnson, Phys. Rev. B **82**, 024435 (2010).

[43]F. E. Wang, W. J. Buehler, and S. Pickart, Jpn. J. Appl. Phys., **36**, 3232 (1965).

[44]Y. Kudoh, M. Tokonami, S. Miyazaki, and K. Otsuka, Acta Metall. **33**, 2049 (1985).

[45]G. D. Ayushina, E. S. Levin, and P. V. Gel'd, Russ. J. Phys. Chem. **43**, 1548 (1969).

[46]D. B. Miracle, Acta Metall. Mater., **41**, 649 (1993).

[47]M. Nolan and S. A. M. Tofail, Biomaterials **31**, 3439 (2010).

[48]L. Sandoval and H. M. Urbassek, Nano Lett. **9**, 2290 (2009).